https://doi.org/10.1007/s41230-026-5163-9

In situ monitoring of surface depressions in metal laser additive manufacturing and its interlayer transfer mechanism

Jie Li[1], *Jie Wan[1,2], Zi-jian Chen[1], Jin-shan Li[1,2], and **Jun Wang[1,2]

1. State Key Laboratory of Solidification Processing, Northwestern Polytechnical University, Xi'an 710072, China

2. Chongqing Innovation Center, Northwestern Polytechnical University, Chongqing 401120, China

Abstract: In laser powder bed fusion (LPBF) additive manufacturing, surface depressions caused by melt pool instability can induce defects throughout the layer-by-layer printing process. To address the limited understanding of interlayer defect transmission mechanisms, synchrotron X-ray in situ imaging was used to systematically investigate the dynamic evolution of surface depressions during multi-pass printing by adjusting interlayer process parameters. Experimental results show that insufficient energy input in the first layer leads to balling and fracture of melt tracks. When the energy input in the second layer is increased, local overheating at the gap between melt tracks from the previous layer causes surface depressions. Reducing the energy input in the third layer hinders melt backflow, enlarging the depression region. Further lowering the energy input in the final layer leads to the formation of internal unfused defects. This study reveals the dynamic correlation between surface depressions and interlayer defect evolution, offering critical experimental evidence and theoretical guidance for closed-loop interlayer process control in laser additive manufacturing.

Keywords: laser powder bed fusion; synchrotron radiation X-ray imaging; cross-layer defects; dynamic regulation

CLC numbers: TG146.23 **Document code:** A **Article ID:** 1672-6421(2026)03-283-08

1 Introduction

Laser powder bed fusion (LPBF) additive manufacturing offers significant advantages in achieving integrated material-structure-performance fabrication due to its unique layer-by-layer process. It has been widely applied in high-end sectors such as aerospace and biomedical engineering[1]. However, complex physical phenomena such as melt flow and phase-change heat transfer cause significant fluctuations in melt pool behavior, leading to various porosity defects, including keyholes, gas pores, and lack of fusion[2]. More importantly, the inherent layer-by-layer nature of LPBF allows these defects to propagate vertically, significantly degrading the component's performance, especially its fatigue life[3]. Therefore, understanding melt flow dynamics and their relationship with defect formation is essential for ensuring component quality[4].

Studies on surface depression defects in melt pools have produced several important findings. Using a three-dimensional transient multiphase model, Pang et al.[5] systematically investigated the effects of environmental pressure and laser power on melt pool morphology. They identified vapor recoil pressure as the main cause of surface depression, with reduced ambient pressure significantly exacerbating the defect. Zheng et al.[6] found that changes in laser scanning speed and powder layer thickness significantly affect melt pool depression characteristics. High scanning speeds tend to cause periodic depressions at the rear of the melt pool. Wang et al.[7] also reported that insufficient laser energy caused multiple beam reflections among powder particles, leading to uneven energy distribution and the formation of unmelted regions and random surface depressions. Collectively, these studies indicate

*Jie Wan

Born in 1992, Ph. D., Associate Professor. Research interest: Laser additive manufacturing of advanced metal materials.

E-mail: wan@nwpu.edu.cn

**Jun Wang

Born in 1984, Ph. D., Professor. Research interest: Solidification science and technology.

E-mail: nwpuwj@nwpu.edu.cn

Received: 2025-07-14; Revised: 2025-11-21; Accepted: 2025-11-25

that surface depressions occur fundamentally from external forces that cause surface deformation of the melt pool. Due to rapid solidification, the molten metal lacks sufficient time to reflow to fill these depression defects. Although optimizing parameters such as laser power and scanning speed can help control melt flow and reduce surface depressions, current studies insufficiently address their impact on the formation quality of subsequent layers.

Investigating the layer-by-layer defect formation process requires advanced characterization techniques. Traditional metallography and X-ray computed tomography (X-CT) can detect final defects but fail to capture their dynamic formation[8]. Although infrared thermography and high-speed imaging provide real-time data on melt pool temperature and surface morphology[6, 7], their utility is constrained by limited penetration depth and spatial resolution[9-11]. In contrast, synchrotron X-ray imaging enables the study of transient melt pool phenomena with submicron spatial and temporal resolution[12]. Synchrotron X-ray imaging has been widely used to investigate defect formation mechanisms during single-pass printing. Hojjatzadeh et al.[13] identified six types of pores during single-pass printing and revealed their formation mechanisms. Simonds et al.[14] and Zhao et al.[15] captured abnormal keyhole formation at the laser start and stop points, respectively. Huang et al.[16] investigated keyhole behavior across stable, unstable, and transitional states. However, single-layer studies often overlook the cumulative effects of interlayer thermal history and surface morphology on subsequent melt pool behavior and defect formation. In recent years, researchers have increasingly focused on defects between multiple layers[17]. Stef et al.[18] used X-CT to show that pores often occur at pass junctions. Leung et al.[19] employed synchrotron X-ray imaging to reveal interlayer wetting and growth mechanisms, finding that a thin powder layer between melt tracks easily leads to lack-of-fusion and interlayer porosity. However, the effect of the depression of the melt pool surface on the generation of defects and interlayer transfer was not discussed.

Utilizing the BL12SW beamline at the Shanghai Synchrotron Radiation Facility, this study enables in situ dynamic observation of the LPBF multi-pass printing process. The interlayer transfer of surface depressions under varying energy densities was systematically studied by adjusting process parameters. Previous studies have reported that depression region significantly influences closed-loop interlayer process control due to increased laser absorption and thermal resistance[20, 21]. This provides critical experimental evidence and theoretical support for achieving high-performance metal additive manufacturing.

2 Experimental methods

2.1 Synchrotron X-ray imaging setup

This experiment was conducted at the BL12SW beamline of the Shanghai Synchrotron Radiation Facility. A custom-built micro-printing system was employed, consisting of a laser optics system, atmosphere control, powder spreading module, and synchronized imaging unit. Figure 1(a) presents a schematic of the powder spreading system, with key components including the molding piston and sample table, and the powder bin with a scraper, as detailed in the sub-panels.

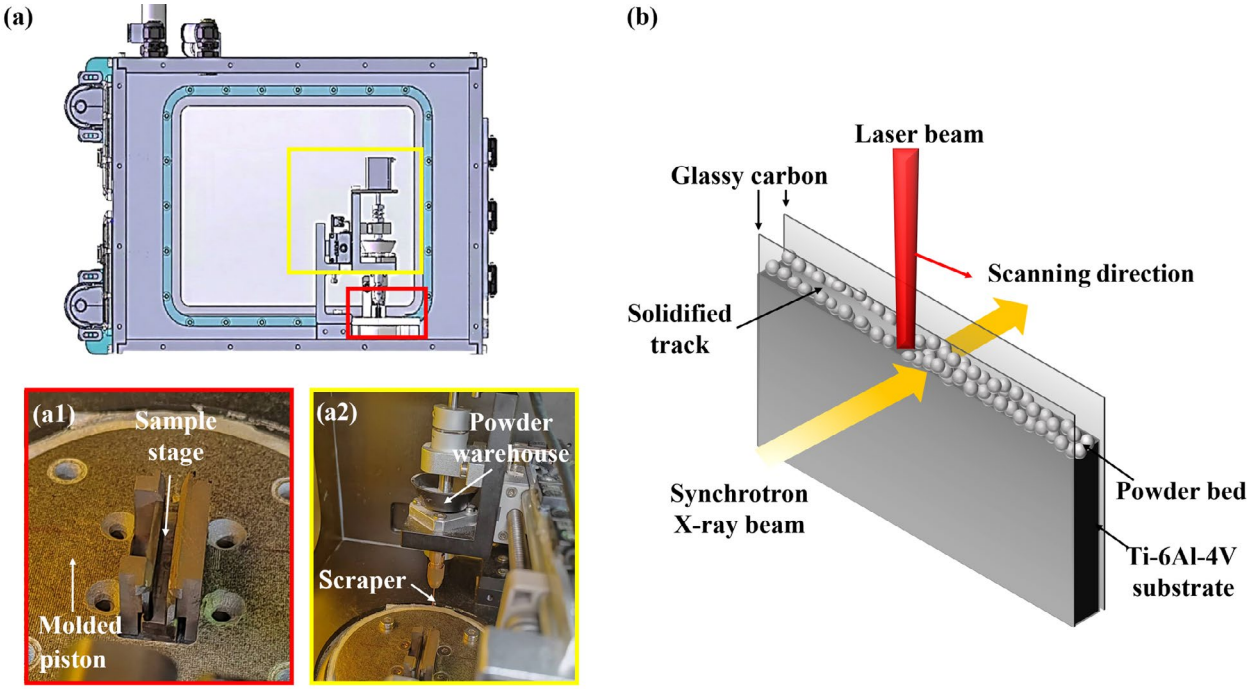

Fig. 1: Schematic diagram of in situ X-ray characterization of LPBF additive manufacturing process: (a) schematic of the powder spreading system; (a1) sample table lifting system; (a2) powder delivery and filling device; (b) schematic of in situ X-ray imaging experiment

A monochromatic X-ray beam (98.76 keV, 0.1255 Å) passed through a grating slit (0.5 mm×0.5 mm) to illuminate the sample. The transmitted X-rays were recorded using a high-speed CMOS camera (exposure time: 10 ms, resolution: 2320×1031, pixel size: 3 μm). A sandwich-structured sample [Fig. 1(b)] was prepared, consisting of a 2 mm-thick Ti-6Al-4V substrate positioned between two 1 mm-thick carbon glass plates.

2.2 Image processing and analysis

The acquired X-ray images were processed using flat-field correction to eliminate artifacts caused by pixel variation and thermal noise during acquisition[19]. Image features were distinguished based on X-ray absorption contrast manifested through grayscale variations. The powder bed interface was identified by abrupt grayscale reduction at the substrate boundary. Melt track contours were determined through global thresholding that captured the grayscale difference between the liquid melt pool exhibiting higher absorption and the surrounding powder or solid material. Surface depressions were tracked as concave gas-liquid interface deformations across sequential frames. Lack-of-fusion defects were identified as regions maintaining powder-like grayscale values while being completely surrounded by solidified material. These analytical methods enabled precise quantification of dimensional parameters, including melt pool dimensions and defect areas, based on the calibrated spatial resolution of 3.0 μm per pixel.

2.3 Materials and processing parameters

The experimental material was gas-atomized Ti-6Al-4V powder (15–53 μm, Xi'an Ouzhong Materials Technology Co., Ltd.). A powder layer thickness of 100 μm was used for each deposition, and the oxygen concentration in the argon atmosphere was maintained below 100 ppm. The substrate was not preheated before printing.

Linear energy density ($E=\frac{P}{V}$, where P is laser power and V is scanning speed) was modulated through laser power and scanning speed variations to study surface cavity evolution and interlayer defect transmission[22]. Parameter selection was guided by preliminary single-track experiments mapping the processing window. Below 10 J·mm^{-1}, discontinuous tracks with severe balling formed, while stable continuous tracks were achieved between 10–25 J·mm^{-1}.

2.4 Experimental design strategy

The selected parameters were thus deliberately chosen from both inside and outside this continuous tracks window to systematically trigger and study specific defect formation mechanisms across layers, as list in Table 1. The first layer at 18.75 J·mm^{-1} was set to induce melt pool spheroidization and create a defective baseline. The second layer at 25 J·mm^{-1} within the stable window examined recoil pressure effects on cavity formation. The third layer at 10 J·mm^{-1} studied high-speed melt flow limitations, and the fourth layer at 7.5 J·mm^{-1} confirmed lack-of-fusion defects under critical energy shortage. This systematic approach revealed how energy variations drive defect development through multiple layers.

Table 1: Process parameters of in situ additive manufacturing experiment

Layer	P (W)	V (mm·s^{-1})	E (J·mm^{-1})	Characteristics	Scientific objective
First	75	4	18.75	Continuous shallow melt track	Induce spheroidization
Second	100	4	25	Stable continuous melt track	Examine recoil pressure effects
Third	100	10	10	Discontinuous melt track	Probe high-speed melt flow recirculation
Fourth	75	10	7.5	Severe balling	Validate the lack-of-fusion formation mechanism

3 Results and discussion

3.1 Surface dimple morphology evolution

3.1.1 Molten pool spheroidization (first layer)

Figure 2 illustrates the dynamic evolution of melt pool morphology during the first-layer printing process, with the laser scanning from right to left. At the initial stage, a low energy input (18.75 J·mm^{-1}) results in balling and a discontinuous melt track. Initially, the powder bed exhibits a distinct interface between the substrate and the powder layer [Fig. 2(a)]. After t+100 ms of laser irradiation [Fig. 2(b)], a vapor cavity forms with a depth of 25.1 μm and a width of 69.4 μm, penetrating less than the full powder bed thickness (100 μm). As shown in Fig. 2(c), the cavity dimensions are reduced (depth: 17.7 μm, width: 42.6 μm), and still insufficient to fully penetrate the powder bed. After printing, the melt track displays pronounced balling, leading to discontinuous and irregular track formation. Ultimately, the melt track evolves into discrete spherical droplets [Fig. 2(d)], with an average curvature radius of 85.5 μm and a contact angle of 134°. Under low energy density, poor melt wettability triggers Rayleigh-Plateau instability, causing the melt track to fragment into discrete droplets accompanied by pronounced surface depressions. These depressions contain numerous partially melted powder particles, further disrupting melt uniformity and hindering thermal conduction in subsequent layers[23].

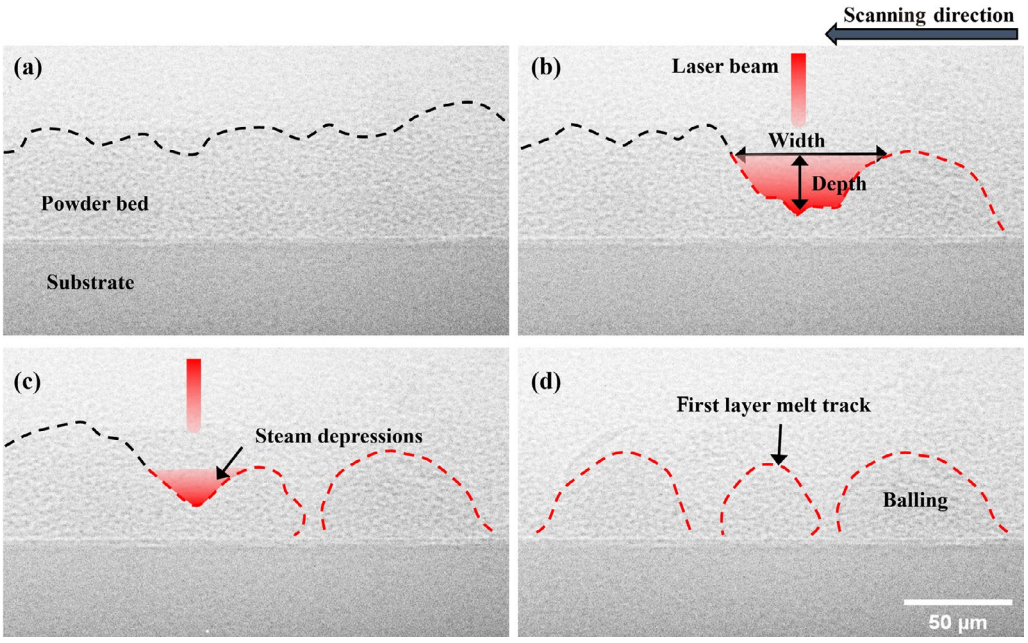

Fig. 2: Morphology evolution of the first-layer melt pool: (a) *t*+0 ms; (b) *t*+100 ms; (c) *t*+200 ms; (d) *t*+300 ms. (The black lines represent the powder bed interface, while the red lines indicate the interface of the solidified melt channel.)

3.1.2 Surface depressions under elevated energy input (second layer)

To compensate for the insufficient energy input in the first layer, the second layer employed an active control strategy by increasing the laser power, raising the energy density to 25 J·mm^{-1} (a 33% increase). This adjustment aimed to investigate the effect of melt pool oscillations on surface depressions under elevated recoil pressure[23, 24], while keeping the powder layer thickness constant at 100 μm. Figure 3(a) shows a shallow vapor cavity (depth 45.3 μm, width 60.2 μm). After *t*+50 ms [Fig. 3(b)], the vapor cavity expands at the balling gap of the first layer, reaching a width of 85.3 μm and a depth of 120.5 μm. At *t*+100 ms [Fig. 3(c)], the vapor cavity deepens further and penetrates into the substrate, with its width narrowing to 70.2 μm.

Figure 3(d) shows the melt track morphology after the second-layer printing, revealing a depression formed between the balling droplets of the first layer, with a depth of 324 μm, a width of 78 μm, and tilt angles of 49.3° (left) and 60.9° (right). Measurements indicate that the actual powder thickness at the depression site [Fig. 3(d)] is approximately 182 μm, significantly exceeding the nominal 100 μm. The accumulation

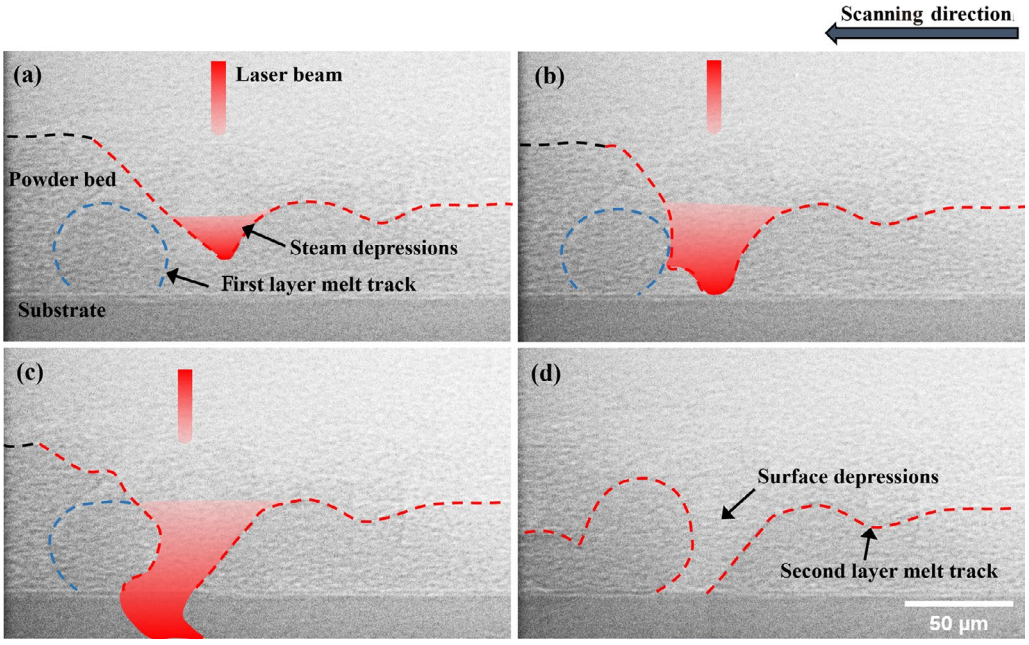

Fig. 3: Morphological evolution of the second-layer melt pool: (a) *t*+0 ms; (b) *t*+50 ms; (c) *t*+100 ms; (d) *t*+250 ms. (The black lines denote the powder bed interface, the blue lines are the surface of the first layer of the melt channel, and the red lines are the surface of the second layer of the melt channel.)

of powder in these depression regions creates localized thermal barriers[25, 26]. The resultant high thermal resistance impedes heat dissipation, leading to localized heat accumulation and overheating. This intense local heating induces material vaporization, where the recoil vapor pressure exceeds the melt's surface tension, driving the formation of deep surface depressions[27, 28].

The dramatic melt pool deepening and fluctuations observed in powder accumulation zones [Figs. 3(b–c)] provide strong evidence of these localized overheating effects. These observations find support in computational studies by Huang et al.[16] and Khairallah et al.[24], which demonstrate that regions with elevated thermal resistance experience enhanced energy confinement, leading to substantial local temperature increases and keyhole instability.

3.1.3 Surface depressions at high scanning rates (third layer)

In the third layer, the scanning speed was increased, reducing the energy density to 10 J·mm^{-1}. As a result, a wide and shallow concave cavity with a narrow tip forms 82 μm to the upper left of the deep pit generated in the second layer (scanning direction: right to left), as shown in Fig. 4. The initial powder layup reveals a powder thickness of 96 μm in the concave region [Fig. 4(a)]. After *t*+50 ms of laser irradiation [Fig. 4(b)], a narrow depression with a depth of 94.2 μm appears in the P1–P2 region. At *t*+100 ms [Fig. 4(c)], the surface depression widens further, and the depth slightly increases above the P2–P3 gap, although it remains significantly less than that above the P1–P2 gap. Figure 4(d) shows the final morphology of the melt track in the third layer, featuring a concave cavity with a depth of 164 μm and a width of 266 μm, and front and rear inclination angles of 74.9° and 71.8°, respectively.

The formation of this irregularly wide and shallow cavity is due to the difference in thermal resistance between thick and thin powders[28, 29]. Higher thermal resistance in thick powder regions intensifies local heat accumulation, potentially forming deep melt zones or even keyholes[16, 26], thereby increasing surface concavity. This effect manifests as the narrow depression between P1 and P2 in Fig. 4(d). In contrast, when the laser traverses a thin powder region, the sudden drop in thermal resistance causes rapid cooling of the melt pool[30]. The rapid solidification and width reduction of the melt pool front during this transition [Figs. 4(b–c)] clearly indicate rapid cooling phenomena. This behavior is characteristic of the melt pool's response to the abrupt change in thermal conductivity between powder beds and solid material[31], as documented in the in situ X-ray observations of Zhao et al[15]. This leads to a shallower penetration depth, increased melt viscosity, and inhibited backflow, ultimately forming a wide concave cavity with a narrow tip.

The leftward shift of the third-layer surface depression results from the combined effects of Marangoni convection and capillary forces induced by the pre-existing depression geometry[32]. Surface depressions constitute regions of negative curvature, which, according to the Young-Laplace equation, generate capillary suction pressures that drive melt flow radially inward toward the depression's center[33]. This inward flow possesses a significant velocity component that directly opposes the laser's scanning direction (from right to left). Consequently, this oppositional flow shifts the melt pool's mass center rearward (to the right) relative to the laser spot's instantaneous position. This mechanism, where capillary forces from depression sidewalls attract molten material and displace the melt pool, is consistent with high-fidelity simulations of melt pool dynamics[24]. The observed shift provides direct experimental validation of this numerically predicted behavior.

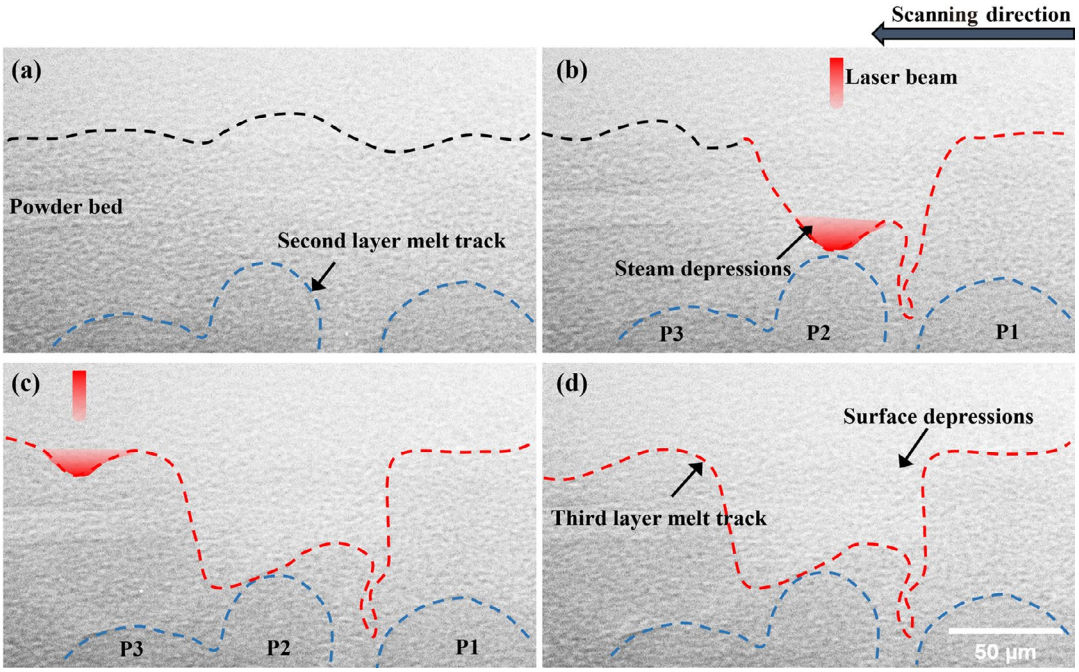

Fig. 4: Morphological evolution of the third-layer melt pool: (a) *t*+0 ms; (b) *t*+50 ms; (c) *t*+100 ms; (d) *t*+150 ms. (The black lines are the powder bed interface, the blue lines are the surface of the second layer of the melt channel, and the red lines are the surface of the third layer of the melt channel.)

3.1.4 Lack of fusion defects (fourth layer)

Although the energy input was reduced in the third layer, it was further decreased in the fourth layer to 7.5 J·mm^{-1} to examine defect evolution resulting from the pores formed previously. In situ observations reveal the formation of lack-of-fusion defects above the surface depression of the third layer and within the fourth layer. As shown in Fig. 5(a), the melt pool exhibits a shallow bowl-like shape, with its base initially contacting the depression area of the third layer. At t+30 ms [Fig. 5(b)], the melt pool fails to fully cover the depression zone, leading to a triangular lack-of-fusion defect (403.5 μm^2). By t+60 ms [Fig. 5(c)], the defect expands to 612.8 μm^2, evolving into a distinctive "swallow-tail" shape.

The combination of powder accumulation and insufficient energy input creates ideal conditions for lack-of-fusion defects. The increased powder volume in depression regions requires greater energy for complete melting, while localized thermal resistance further impedes heat transfer[28, 30]. When energy input is inadequate (7.5 J·mm^{-1}), the melt pool cannot penetrate the accumulated powder zone, resulting in the characteristic triangular defects observed in Fig. 5. This mechanism is consistent with recent findings on defect formation in irregular powder beds.

According to the Rosenthal model[24], the melt pool depth, d, is estimated as: $d=\frac{AP}{K(T_m-T_0)\sqrt[3]{V}}$, P is the laser power (75 W), K is the thermal conductivity [6.7 W·(m·K)$^{-1}$], T_m is the melting point (1,923 K), T_0 is the preheating temperature (298 K), V is the scanning speed (10 mm·s^{-1}), and A is the modification factor (0.04). Based on these parameters, the melt pool depth is estimated to be 27.5 μm. However, the actual powder thickness reaches 234 μm in depression zones. Consequently, the melt pool fails to penetrate this thickened powder layer, inevitably forming lack-of-fusion defects approximately 190 μm below the surface [Fig. 5(d)].

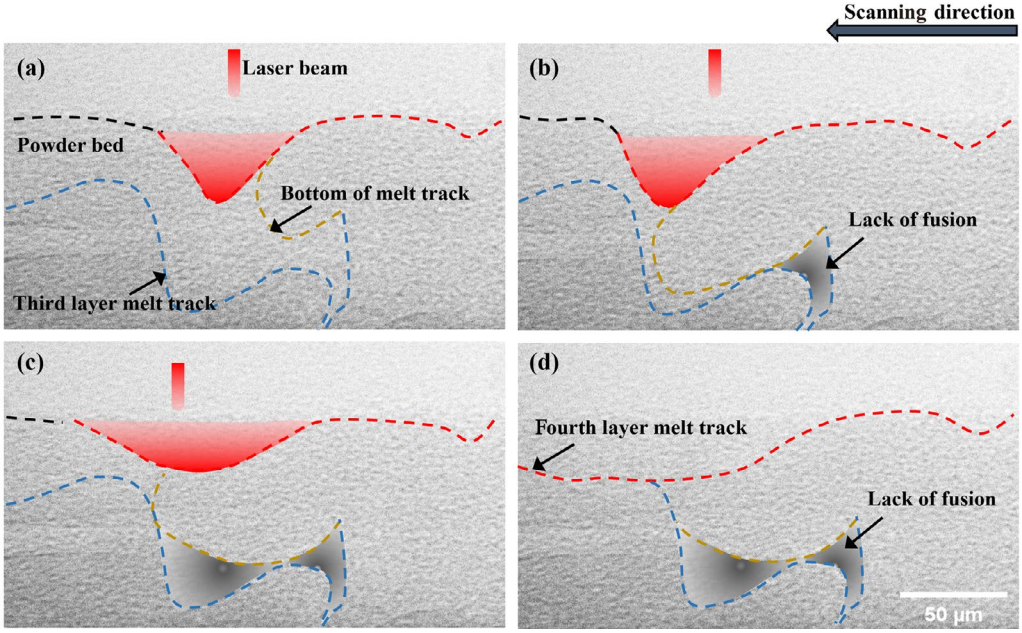

Fig. 5: Morphological evolution of the fourth-layer melt pool: (a) t+0 ms; (b) t+30 ms; (c) t+60 ms; (d) t+90 ms. (The black lines are the powder bed interface, the blue lines are the surface of the third layer of the melt channel, the red lines are the surface of the fourth layer of the melt channel, and the yellow line is the bottom of the fourth layer of the melt channel.)

3.2 Cross-layer transfer mechanism of pore defects

Figure 6 illustrates the interlayer transition process during layer-by-layer printing under varying energy inputs. This transition progresses from melt pool spheroidization to narrow surface depressions, to wide and shallow concave cavities, and ultimately to lack-of-fusion defects. The evolution is primarily driven by abrupt changes in energy input, coupled with surface irregularities.

The mechanisms of thermal resistance variation and their effect on melt pool behavior, as detailed in Sections 3.1.2 and 3.1.3, govern the interlayer defect transfer process. In contrast, in shallow powder regions, reduced laser absorption accelerates melt pool solidification and limits penetration depth, increasing the risk of lack-of-fusion defects. Intrinsic laser fluctuations lead to inherent surface irregularities on the melt track[34]. Consequently, subsequent powder layers exhibit periodic variations between thick and thin regions, causing surface morphology fluctuations in the printed layers. Under low energy input, these fluctuations are exacerbated by spheroidized and fragmented melt tracks. Under active control, increasing the energy input in the next layer deepens the melt pool, which interacts with the underlying geometric features and further degrades surface quality. Conversely, when energy input is actively reduced, if the melt pool continues to penetrate the powder layer, surface

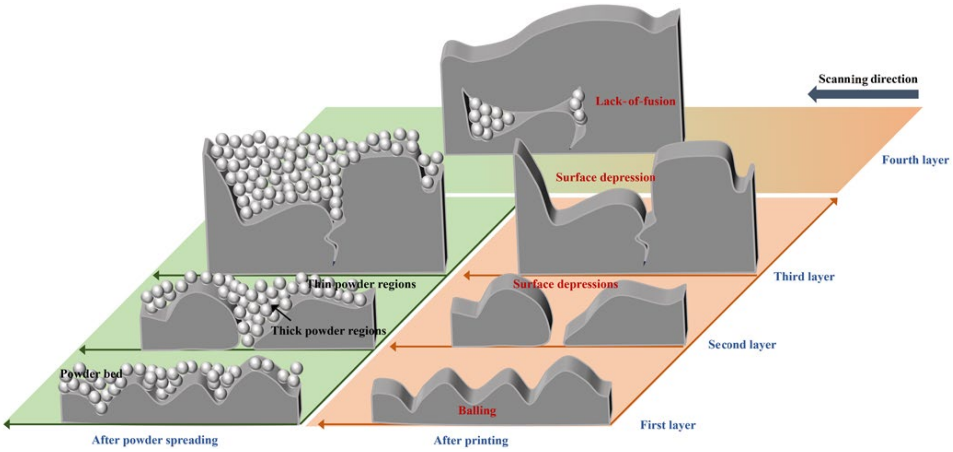

Fig. 6: Morphology of melt tracks and surface depressions after completion of printing from the first to fourth layers

depressions can still form in thick powder regions. If the melt pool fails to penetrate the powder layer, unmelted powder in surface depressions results in internal lack-of-fusion defects. Notably, variations in the radius of curvature of surface depressions alter the melt wetting direction. Capillary forces generated by the depression sidewalls draw the melt backward (against the scanning direction), causing a shift in the melt pool position.

4 Conclusions

This study employed in situ synchrotron X-ray imaging to investigate the mechanisms underlying interlayer defect evolution induced by parameter variations in laser powder bed fusion (LPBF). The key findings are summarized as follows:

(1) Variations in interlayer energy input govern defect morphology evolution. Low energy input in the initial layer leads to spheroidized surface features. Subsequent increases in energy cause localized overheating and surface depressions. In the third layer, a high scanning speed restricts melt flow, enlarging the depressions. Reduced power in the final layer leaves residual porosity within these depressions.

(2) Coupling of energy mutations and interlayer morphology governs defect propagation: Variations in thermal resistance and laser absorption between thick and thin powder regions cause distortions in the temperature field. This leads to localized overheating in thick powder areas, increasing melt pool depth, and resulting in surface depressions.

(3) Surface morphology influences melt wetting behavior. Capillary forces from the sidewalls of surface depressions redirect melt flow opposite to the scanning direction, causing the melt pool to shift. As a result, surface depressions gradually migrate along the scanning path.

Although this investigation employs Ti-6Al-4V, the underlying physical principles governed by variations in local thermal resistance, capillary force-driven melt flow, and energy input-defect correlations are fundamental to LPBF physics and are expected to apply to a broad range of metal alloy systems. While material-specific properties such as surface tension, thermal conductivity, and solidification range will influence specific energy thresholds and defect distributions. The overarching framework of defect transfer governed by the coupling between energy input and interlayer morphology provides a universal basis for understanding and controlling cross-layer defects in laser additive manufacturing.

It should be noted that the layer interval time in this study was set at about 60 s to meet synchrotron imaging needs, which exceeds typical industrial LPBF process times. While this longer interval helps separate the effects of energy input and morphology from rapid heat accumulation[35-37]. Future work should examine how layer interval thermal management and energy input strategies work together.

Acknowledgments

This work was supported by the National Key Research and Development Program of China (No. 2022YFB3707103), the National Natural Science Foundation of China (No. 52301197), the Research Fund of the State Key Laboratory of Solidification Processing (NPU), China (No. 2024-TS-06), the Young Talent Fund of Xi'an Association for Science and Technology (No. 959202413014), and the Fundamental Research Funds for the Central Universities (No. D5000240144).

Conflict of interest

Authors declare that they have no potential conflict of interest.

References

[1] Gu D, Shi X, Poprawe R, et al. Material-structure-performance integrated laser-metal additive manufacturing. Science, 2021, 372(6545): 1–15.
[2] Niu Z, He C, Yang Z, et al. Dynamics of molten droplet/pool fusion in additive manufacturing. Acta Mech. Sin., 2025, 42(3): 325020.
[3] Javidrad H, Bahattin K, Hakan B, et al. Fatigue performance of metal additive manufacturing: A comprehensive overview. Virtual Phys. Prototyp., 2024, 19(1): 5–22.

[4] Wang J, Zhu R, Liu Y, et al. A review on in-situ monitoring and quality control for laser powder bed fusion. Adv. Powder Mater., 2023, 2(4): 100137.
[5] Pang S, Chen X, Zhou J, et al. 3D transient multiphase model for keyhole, vapor plume, and weld pool dynamics in laser welding, including the ambient pressure effect. Opt. Laser Eng., 2015, 74: 47–58.
[6] Zheng M, Wei L, Chen J, et al. A novel method for the molten pool and porosity formation modelling in selective laser melting. Int. J. Heat Mass Transf., 2019, 140: 1091–1105.
[7] Wang C H, Fu S Y, Kung L J, et al. Combustion and microexplosion of collision-merged methanol/alkane droplets. Proc. Combust. Inst., 2005, 30(2): 1965–1972.
[8] Ziabari A, Venkatakrishnan S V, Snow Z, et al. Enabling rapid X-ray CT characterisation for additive manufacturing using CAD models and deep learning-based reconstruction. npj Comput. Mater., 2023, 9(1): 91.
[9] Myers A J, Quirarte G, Beuth J L, et al. Two-color thermal imaging of the melt pool in powder-blown laser-directed energy deposition. Addit. Manuf., 2023, 78(25): 103855.
[10] Bidare P, Bitharas I, Ward R M, et al. Fluid and particle dynamics in laser powder bed fusion. Acta Mater., 2018, 142: 107–120.
[11] Zhao J, Yang Z, Chen Q, et al. Real-time detection of powder bed defects in laser powder bed fusion using deep learning on 3D point clouds. Virtual Phys. Prototyp., 2025, 20(1): e2449171.
[12] Khairallah S A, Martin A A, Lee J R I, et al. Controlling interdependent meso-nanosecond dynamics and defect generation in metal 3D printing. Science, 2020, 368(6491): 660–665.
[13] Hojjatzadeh S M H, Parab N D, Guo Q, et al. Direct observation of pore formation mechanisms during LPBF additive manufacturing process and high-energy-density laser welding. Int. J. Mach. Tool Manuf., 2020, 153: 103555.
[14] Simonds B J, Tanner J, Artusio-Glimpse A, et al. The causal relationship between melt pool geometry and energy absorption measured in real time during laser-based manufacturing. Appl. Mater. Today, 2021, 23: 101049.
[15] Zhao C, Fezzaa K, Cunningham R W, et al. Real-time monitoring of laser powder bed fusion process using high-speed X-ray imaging and diffraction. Sci. Rep., 2017, 7: 3602.
[16] Huang Y, Fleming T G, Clark S J, et al. Keyhole fluctuation and pore formation mechanisms during laser powder bed fusion additive manufacturing. Nat. Commun., 2022, 13(1): 1170.
[17] Chen Y, Clark S J, Leung C L A, et al. In situ X-ray imaging of defect formation dynamics in laser powder bed fusion. Appl. Mater. Today, 2020, 20: 100650.
[18] Stef J, Poulon-Quintin A, Redjaimia A, et al. Mechanism of porosity formation and influence on mechanical properties in selective laser melting of Ti-6Al-4V parts. Mater. Des., 2018, 156: 480–493.
[19] Leung C L A, Marussi S, Atwood R C, et al. In situ X-ray imaging of defect and molten pool dynamics in laser additive manufacturing. Nat. Commun., 2018, 9: 1355.
[20] Cai Y, Xiong J, Chen H, et al. Machine learning for process optimization and quality control in additive manufacturing: A review. J. Manuf. Syst., 2023, 70: 309–326.
[21] Feng S, Chen Z, Bircher B, et al. A review on powder spreading in laser powder bed fusion additive manufacturing: Mechanisms, modelling and future outlook. Mater. Des., 2022, 222: 111115.
[22] King W E, Anderson A T, Ferencz R M, et al. Laser powder bed fusion additive manufacturing of metals: Physics, computational, and materials challenges. Appl. Phys. Rev., 2015, 2(4): 610–644.
[23] Wei L C, Ehrlich L E, Powell-Palm M J, et al. Thermal conductivity of metal powders for powder bed fusion additive manufacturing. Addit. Manuf., 2018, 21: 201–208.
[24] Khairallah S A, Anderson A T, Rubenchik A, et al. Laser powder-bed fusion additive manufacturing: Physics of complex melt flow and formation mechanisms of pores, spatter, and denudation zones. Acta Mater., 2016, 108: 36–45.
[25] Gusarov A V, Yadroitsev I, Bertrand P, et al. Heat transfer modelling and stability analysis of selective laser melting. Appl. Surf. Sci., 2007, 254(4): 975–979.
[26] Hyer H C, Petrie C M. Melt pool dynamics and defect formation in laser powder bed fusion: A review of in-situ process monitoring. J. Manuf. Process, 2022, 76: 666–674.
[27] Calta N P, Wang J, Kiss A M, et al. An instrument for in situ time-resolved X-ray imaging and diffraction of laser powder bed fusion additive manufacturing processes. Rev. Sci. Instrum., 2018, 89(5): 055101.
[28] Lupo G, Niemann M, Goniva C, et al. Multi-physics modelling of thermal and fluid dynamics in laser powder bed fusion with experimental validation. Results Phys., 2024, 67: 108043.
[29] Li E, Zhou Z, Wang L, et al. Numerical analysis of powder spreading in additive manufacturing: Influence of particle size and distribution on packing density. Powder Technol., 2022, 397: 117012.
[30] Scipioni B U, Guss G, Wu S, et al. An experimental and numerical investigation of the effect of process parameters on melt pool characteristics in laser powder bed fusion. Mater. Des., 2017, 135: 385–396.
[31] Sun J, Guo M, Shi K, et al. A comprehensive review on defect detection in metal additive manufacturing based on machine learning. MSAM, 2022, 1(1): e2022001.
[32] Pang J, Huang L, Liu H, et al. In-situ monitoring and closed-loop control of microstructure in laser additive manufacturing. Mater. Des., 2025, 254: 114043.
[33] Rubenchik A, Wu S, Mitchell S, et al. Metal 3D printing with laser-based powder bed fusion: Modeling and experimental validation. Appl. Opt., 2015, 54(11): 7230–7233.
[34] Ren Z, Gao L, Clark S J, et al. Machine learning-aided real-time detection of keyhole pore generation in laser powder bed fusion. Science, 2023, 379(6627): 89–94.
[35] Mohr G, Altenburg S J, Hilgenberg K. Effects of interlayer time and build height on resulting properties of 316L stainless steel processed by laser powder bed fusion. Addit. Manuf., 2020, 32: 101080.
[36] Babacan N, Yildiz M T, Ozdemir F, et al. The effect of interlayer time on the microstructure and mechanical properties of a Co-Cr alloy produced by laser powder bed fusion. J. Alloys Compd., 2025, 1036: 181661.
[37] Medvedev A E, Brudler S, Piegert S, et al. Effect of interlayer processing delays on microstructure and mechanical properties of Ti-6Al-4V produced by laser powder bed fusion. J. Mater. Process. Technol., 2025, 340: 118032.